

Prediction of the structure and refractive index profile of fused fiber-optic components: A numerical and experimental study

Avihai Spizzichino ¹, Sharone Goldring,² and Yuri Feldman ¹

¹Department of Mechanical Engineering, Ben-Gurion University of the Negev, PO. Box 653, Beer-Sheva 8410501, Israel

²Applied Physics Division–Soreq NRC, Yavne 81800, Israel



(Received 5 October 2020; accepted 7 January 2021; published 27 January 2021)

We report a generic theoretical framework for accurate simulation of the temporal and spatial evolution of fused fiber-optic components, fabricated by the “heat and pull” technique. The methodology is based on the solution of quasi-3D incompressible Navier-Stokes equations formulated for immiscible two-phase flow. The two-phase interface is resolved by employing an interface tracking approach combined with the immersed boundary method. The model facilitates accurate spatiotemporal prediction of the evolution of both the external shape of the optical component and the internal dopant concentration during fabrication. Validation of the model was obtained by extensive comparison to experimental results. The model was found to be a convenient theoretical tool that may reliably facilitate the design and fabrication process of a wide spectrum of optic components.

DOI: [10.1103/PhysRevE.103.013315](https://doi.org/10.1103/PhysRevE.103.013315)

I. INTRODUCTION

Fiber-optic components have diverse structures and applications, ranging from simple 2×2 symmetric couplers, through fiber-laser pumps and signal combiners, to even more complex systems, such as photonic lanterns [1,2]. Many of these fiber-optic components are fabricated by the so-called “heat and pull” technique, in which optical fibers are fused and tapered simultaneously. The popularity of the technique may be attributed to the simplicity of the setup and the ability to fabricate a wide range of optical components that accurately meet a variety of design requirements. The “heat and pull” technique includes three fundamental steps: gathering and arranging the optical fibers in a particular initial order, subjecting the fibers to viscous flow sintering, and subsequently pulling the fibers. This production process affects both the external geometry of the produced fiber-optic component and the distribution of the internal dopant concentration. The functionality of fused fiber-optic components thus depends on their structure and the concentration profile of the inner dopants. A number of models and simulation tools predicting the optical functionality and the light transmission characteristics of particular fiber components have been developed over the years and are well established today [3–5]. However, all the developed tools require the precise geometry of the given fiber component as input. Without this information, the result of any modeling tool will not be sufficiently accurate. This drawback becomes particularly critical for complex combiners whose light transmission characteristics are especially sensitive to the geometry of the component and the concentration profile of the internal dopants. Therefore, the development of complex fiber components typically requires conducting a series of preliminary onsite experiments, which can significantly lengthen R&D times and increase production costs.

We now briefly review some of the main studies that have focused on modeling the structure of fiber-optic components. Lacroix *et al.* [6] empirically approximated the cross-sectional shape of two identical fused fibers by imposing the principle of conservation of matter. However, this approach is limited and does not allow for addressing other critical phenomena, such as deformation of the optical component and diffusion of the dopants within the component core, or for predicting the fusion characteristics of the optical components produced from initially more complicated structures. Other research groups have tackled the problem by developing models based on solving the Navier-Stokes (NS) equations. The studies of Garabedian [7] and Richardson [8–10], for example, analyzed the dynamic plane Stokes flow of a viscous incompressible fluid bounded by a smooth closed curve driven solely by the surface tension force. Their analysis was based on conformal mapping and predicted the shape evolution as a function of the fusion rate. Hopper [11–13] developed an advanced model predicting the temporal evolution of the component’s shape by using conformal mapping in the complex z plane. However, this method required the assumption of a parametric form based on approximation shape functions, and it thus cannot be applied to optic fiber components of arbitrary initial geometry.

Of particular interest are the studies of Pone *et al.* [14,15], who investigated the refractive index profile of fused optic fiber coupler cross sections. They presented numerical simulations that were based on the solution of continuity and NS equations as well as a convection-diffusion equation for the dopant concentration field. In contrast to previous studies that addressed only the evolution of the external shape of fiber-optic components by a conformal mapping technique [11,10,16], those authors resolved the time evolution of the dopant concentration inside the fibers. Despite progress in simulations of fiber-optic components and the excellent agreement between the numerical and experimental measurements

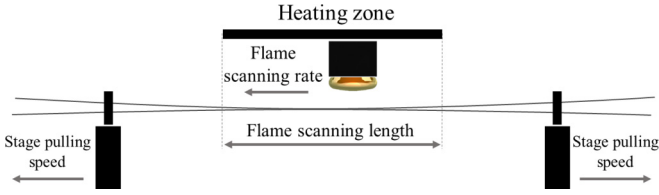


FIG. 1. Schematic diagram of the fibers' coupling process.

presented by Pone *et al.* [14], a generic tool to simulate the structure and the refractive index distribution of complex fused fiber components is not readily available. The need for the development of a high-fidelity structural simulation tool for facilitating the fabrication of components is particularly evident for complex systems whose fabrication is challenging due to their high optical sensitivity to tiny structural variations.

The current study focuses on the development of a theoretical framework based on the numerical solution of quasi-three-dimensional (3D) incompressible NS equations formulated for immiscible two-phase flow. The two-phase interface is resolved by employing an interface tracking approach combined with the immersed boundary method. The developed methodology was extensively validated experimentally and constitutes a convenient numerical tool for accurate prediction of both the external geometry and the composition of the internal core for a vast variety of optical components.

II. THEORETICAL FRAMEWORK

The fabrication of fiber couplers by the heat and pull technique requires a heat source (a hydrogen flame in our case) and stages to hold and pull the fibers. The tapering rate is determined by the pulling speed and the temperature distribution of the heated zone. The temperature distribution during the process is, in turn, controlled by the flame intensity, the flame to fiber distance, and the flame scanning rate and length. To obtain an effective isothermal heating zone, the flame scanning rate must be much higher than the rate of fiber pulling. Providing that the above conditions are maintained, the active heating zone is equivalent to the flame scanning length. In summary, the flame scanning length determines the heating zone, and the stage pulling speed controls the tapering rate (see Fig. 1).

Typically, the process occurs at a steady temperature lying in the range of 1200–1900 °C, at which the viscous sintering of the fibers may be regarded as the motion of an incompressible Newtonian fluid driven by surface tension [14] and damped by viscous dissipation forces. Although the system under consideration is three dimensional in practice, the fiber coupling process can be approximated by a transient quasi-3D model. The third axial direction along the tapered coupler is replaced by a series of discrete axial cross sections of different areas. This approximation is acceptable in the case of an isothermally heated zone, which is a good approximation for the flame scanning setup, as long as the pulling rate is much lower than the scanning rate. Each such cross section comprises the local structure of the glass coupler whose shape had formed as the coupler was drawn through the heated zone. As

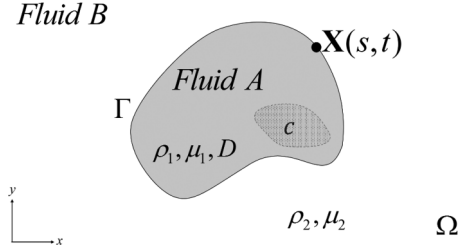


FIG. 2. Schematic representation of a two-phase flow configuration.

long as the pulling rate remains constant, each cross section can be related to the discrete time at which the coupler had formed and had remained “frozen” immediately after it had been drawn out of the hot zone.

The decrease of the cross-sectional area $A(t)$ taking place at time t as a result of simultaneous heating and drawing out of the coupler in the heated zone is related to the constant pulling rate v_s and the flame scanning length l , by the following ordinary differential equation:

$$\frac{d}{dt}A(t) + \frac{2v_s}{l}A(t) = 0, \quad (1)$$

whose analytical solution provides an expression for the decrease with time in cross-sectional area $A(t)$:

$$A(t) = A_0 e^{-(2v_s t/l)}, \quad (2)$$

where A_0 is the initial cross-sectional area of the fibers forming the coupler. The decrease in the cross-sectional area of the coupler can be formulated by introducing a volumetric sink, q , defined as

$$q = -\frac{2v_s \rho(\mathbf{x})}{l}. \quad (3)$$

Equation (3) will be utilized in the following sections when describing the fluid dynamics of the fabrication process of fiber couplers.

III. GOVERNING EQUATIONS

Consider two incompressible viscous fluids A and B confined by a rectangular domain, where the fluid B surrounds fluid A and the two fluids are separated by a sharp closed interface Γ parametrized by $X(s, t)$, as shown in Fig. 2. In the context of the present study, fluid A is related to the viscous fused silica and represents the cross section of the fiber coupler, whereas fluid B is related to the surrounding air.

The two fluids have different densities and viscosities represented by $\rho_{1,2}$ and $\mu_{1,2}$, respectively. Fluid A is enriched with dopants to provide the requisite optical characteristics. The concentration distribution of the dopants c is controlled by convection and a constant diffusion coefficient D , and it is assumed that there is no diffusion between fluids A and B . Three equations govern the fluid dynamics of the described system, namely, the continuity, NS, and the dopant

concentration convection-diffusion equations:

$$\rho(I)\nabla \cdot \mathbf{u} = q, \quad (4)$$

$$\rho(I)\left(\frac{\partial \mathbf{u}}{\partial t} + \mathbf{u} \cdot \nabla \mathbf{u}\right) = -\nabla p + \nabla \cdot (\mu(I)(\nabla \mathbf{u} + (\nabla \mathbf{u})^T)) + \frac{1}{3}\mu(I)\nabla(\nabla \cdot \mathbf{u}) + \mathbf{f}, \quad (5)$$

$$\frac{\partial c}{\partial t} + (\mathbf{u} \cdot \nabla)c = D\nabla^2 c, \quad (6)$$

where $\mathbf{u}(u, v)$, p , c , t , \mathbf{f} , and q represent the velocity, pressure, dopant concentration, time, surface tension force density, and volumetric mass source, respectively. Note that because of the spatiotemporal variation of the viscosity, the governing equations (4)–(6) are presented and then solved in dimensional form. (This approach also subsequently facilitates the calibration and fine-tuning of the developed numerical methodology to the experiments.) Nonetheless, all the further postprocessing of the obtained results is rendered dimensionless. Note also that we assume no diffusion between the surrounding air and the fused silica on the fused silica–air interface. The above assumption is in agreement with the study of Ref. [17], who reported that the extent of interfacial ordering at the silica–air interface is on the order of several molecular diameters. The same conclusion can be drawn by simply utilizing 1D diffusion equation with the value of diffusion coefficient $D \sim O(10^{-9}) \text{ m}^2 \text{ s}^{-1}$ typical of

hydrogen in fused silica at high temperatures as estimated by Ref. [18]. By plugging the above value of D within analytical solution of 1D diffusion equation it can be assessed that somewhat recognizable penetration of hydrogen within the core of silica fiber is observed over a timescale of weeks, whereas the overall duration of the production process is about 2 h. As such, diffusion phenomenon can be safely neglected on the fused silica–air interface.

The indicator function, $I(\mathbf{x}, t)$ [19], is a nondimensional scalar field, whose values lie within the range $I \in [0, 1]$. The indicator function is used for representing the spatial distribution of the material properties $[\rho(I), \mu(I)]$ and is used to smear their discontinuity in the vicinity of the sharp interface Γ separating the two fluids. We now define the gradient of the indicator function as

$$\nabla I(\mathbf{x}, t) = \int_{\Gamma} \mathbf{n}[X(s, t)]\delta^2[\mathbf{x} - X(s, t)]ds, \quad (7)$$

where $\mathbf{n}[X(s, t)]$ is a unit vector normal to the interface Γ at point $X(s, t)$ parametrized by $0 \leq s \leq L$ (L is the total length of the interface). The values of I are obtained by solving Poisson's equation:

$$\Delta I(\mathbf{x}, t) = \nabla \cdot \int_{\Gamma} \mathbf{n}[X(s, t)]\delta^2[\mathbf{x} - X(s, t)]ds, \quad (8)$$

where the 2D convolution function δ^2 is obtained by multiplication of two 1D discrete Dirac delta functions d of the form

$$d(r) = \begin{cases} \frac{1}{3\Delta r} \left(1 + \sqrt{-3\left(\frac{|r|}{\Delta r}\right)^2 + 1}\right) & \text{for } |r| \leq 0.5\Delta r, \\ \frac{1}{6\Delta r} \left(5 - 3\frac{|r|}{\Delta r} - \sqrt{-3\left(1 - \frac{|r|}{\Delta r}\right)^2 + 1}\right) & \text{for } 0.5\Delta r \leq |r| \leq 1.5\Delta r, \\ 0 & \text{otherwise,} \end{cases} \quad (9)$$

introduced by Roma *et al.* [20] and verified elsewhere [21–26]. Here Δr is the cell width in the r direction. The obtained values of $I(\mathbf{x}, t)$ are then utilized to update the spatiotemporal variation of the ρ and μ fields:

$$[\rho, \mu](I(\mathbf{x}, t)) = [\rho_1(t), \mu_1(t)] + ([\rho_2(t), \mu_2(t)] - [\rho_1(t), \mu_1(t)])I(\mathbf{x}, t). \quad (10)$$

The surface tension force density, $\mathbf{f}(\mathbf{x}, t)$, appearing in the right-hand side (RHS) of Eq. (5), is related to the local curvature of the interface $\frac{\partial^2 X(s, t)}{\partial s^2}$ as

$$\mathbf{f}(\mathbf{x}, t) = \int_{\Gamma} \sigma \frac{\partial^2 X(s, t)}{\partial s^2} \delta^2[\mathbf{x} - X(s, t)]ds, \quad (11)$$

where σ is the surface tension coefficient.

IV. NUMERICAL METHOD

The numerical methodology utilized in the present study is based on the immersed boundary method, specifically developed for the simulation of two-phase immiscible flows [21]. For the sake of completeness, a brief description of the method follows. In the developed methodology, the enforcing surface tension density \mathbf{f} is treated implicitly and serves as a Lagrange

multiplier, applied to enforce the kinematic constraint of the immiscibility of the two fluids to preserve the sharp interface between the two phases.

The position of the interface is updated by employing the interface tracking approach [27,28]. Following Eq. (11), implicit treatment of the surface force density \mathbf{f} leads to the introduction of additional unknowns ($\partial^2 X / \partial s^2$, $\partial^2 Y / \partial s^2$), which requires the addition of supplementary equations to achieve closure of the overall set of equations:

$$\left(\frac{\partial^2 X_s}{\partial s^2}\right) = \frac{(X_{s+1}^{n+1} - 2X_s^{n+1} + X_{s-1}^{n+1})}{(\Delta s)^2}, \quad (12)$$

$$X_s^{n+1} = X_s^n + \Delta t \int_{\Omega} \mathbf{u}^{n+1} \delta^2(X_s^n - x) dx dy. \quad (13)$$

Substitution of X_{s-1}^{n+1} , X_s^{n+1} and X_{s+1}^{n+1} defined by Eq. (13) into Eq. (12) and moving all the terms known from the previous time step to the RHS yields

$$\frac{\Delta t \int_{\Omega} \mathbf{u}^{n+1} [\delta^2(X_{s+1}^n - x) - 2\delta^2(X_s^n - x) + \delta^2(X_{s-1}^n - x)] dx dy}{(\Delta s)^2} - \left(\frac{\partial^2 X_s}{\partial s^2}\right) = -\frac{X_{s+1}^n - 2X_s^n + X_{s-1}^n}{(\Delta s)^2}. \quad (14)$$

The system of equations (4), (5), and (14) can now be written in a block-matrix form as

$$\begin{bmatrix} H_u & H_{uv} & -\nabla_p^x & \sigma \delta^2(\mathbf{X}(s, t^n) - \mathbf{x}) & 0 \\ H_{vu} & H_v & -\nabla_p^y & 0 & \sigma \delta^2(\mathbf{X}(s, t^n) - \mathbf{x}) \\ \nabla_u^x & \nabla_v^y & 0 & 0 & 0 \\ IC_x & 0 & 0 & -1 & 0 \\ 0 & IC_y & 0 & 0 & -1 \end{bmatrix} \times \begin{bmatrix} u^{n+1} \\ v^{n+1} \\ p \\ \left(\frac{\partial^2 X}{\partial s^2}\right) \\ \left(\frac{\partial^2 Y}{\partial s^2}\right) \end{bmatrix} = \begin{bmatrix} RHS_u^{n-1, n} \\ RHS_v^{n-1, n} \\ RHS_s^n \\ RHS_X^n \\ RHS_Y^n \end{bmatrix}, \quad (15)$$

where $H = \nabla \cdot [\mu(I)(\nabla + \nabla^T)] + \frac{1}{3}\mu(I)\nabla(\nabla) - \frac{3\rho(I)}{2\Delta t}\mathbf{I}$ are Helmholtz operators acting on the u and v velocity components, \mathbf{I} is the identity matrix, and ∇^x ∇^y are the first derivatives in the x and y directions, respectively. IC is the ‘‘interface curvature’’ operator appearing as the first term of Eq. (14). The RHS is defined as

$$RHS_{u,v} = \rho(I) \left[(\mathbf{u} \cdot \nabla) \mathbf{u} - \frac{2}{\Delta t} \mathbf{u} \right]^n + \frac{1}{2\Delta t} \mathbf{u}^{n-1}, \quad (16)$$

$$RHS_{X,Y} = -\frac{X_{s+1}^n - 2X_s^n + X_{s-1}^n}{(\Delta s)^2}, \quad (17)$$

$$RHS_s = \begin{cases} -\frac{2v_s \rho(x)}{l}, & \text{within fluid A} \\ 0, & \text{otherwise} \end{cases}. \quad (18)$$

All the discrete operators were obtained by applying a second-order backward finite-difference scheme for the temporal discretization and by utilizing the standard second-order conservative finite-volume method [29] for the staggered grid spatial discretization. Additionally, all the linear terms were treated implicitly, and all the nonlinear terms were treated explicitly and appear in the RHS. The convection-diffusion equation (6) was solved separately from all the other equations by using the velocity field from the previous time substep. The equation was solved only for the fluid domain A with a zero gradient boundary condition on the interface Γ (see Fig. 2).

To conclude, each computational time step consisted of three main substeps: The first one was the solution to Poisson’s equation, given by Eq. (8). The obtained indicator function $I(\mathbf{x}, t)$ was then used in Eq. (10) to identify the spatial distribution of the μ and ρ fields. In the second substep, the system of equations (15) was solved implicitly by a direct multifrontal massively parallel solver [30,31] to obtain the fully coupled velocity and pressure fields. Finally, in the third step, diffusion equation (6) was solved to obtain the concentration of dopants c , under the assumption of one-way coupling (i.e., no dependence of the flow ρ and μ fields on the concentration of dopants), and the interface position was updated by utilizing Eq. (13). The whole procedure was then repeated for the next time step.

V. VALIDATION STUDY

Validation of the numerical methodology was first performed by comparison with previously published test cases.

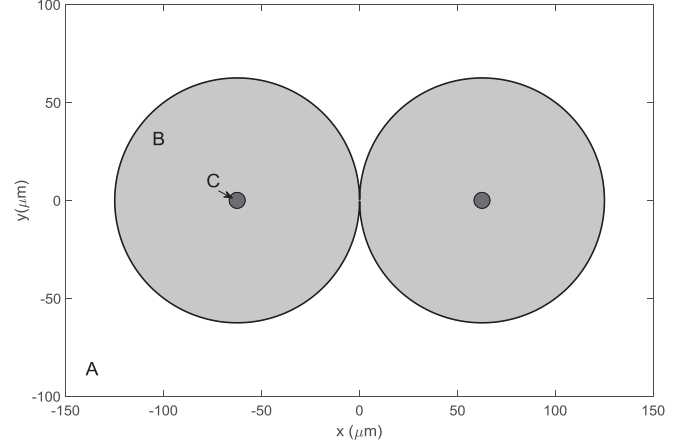


FIG. 3. Initial configuration of two SMF28 fibers. A , B , and C represent air, the fused silica fibers, and the concentration of dopants, respectively.

Experiments specifically designed to test different aspects of the code were then conducted and analyzed.

The 2D immersed boundary method utilized in the present work is not restricted to simulation of the fusion of optical fibers. Indeed, it can provide solutions to a variety of problems involving viscous fluid dynamics. A comparison to previously published benchmarks under different conditions was presented in an earlier publication [21]. Here we restrict the discussion to the fusion dynamics of optical fibers and begin with a comparison with the results obtained by *Pone et al.* [14], who simulated and studied experimentally the fusion of two SMF28 fibers, 125 μm in diameter (as shown in Fig. 3). The fibers were brought into contact and heated with a propane microtorch at a temperature of about 1400 $^\circ\text{C}$.

A structure identical to the one tested in Ref. [14] was simulated by plugging in the same environmental and material conditions and setting the pulling speed v_s to zero. The degree of fusion and the external shape of the fused fibers were then deduced and compared. The degree of fusion without pulling as defined in Ref. [14] is given by

$$f(v_{\text{pull}} = 0) = \frac{W_0 - W(t)}{W_0 - W_\infty}, \quad (19)$$

where W_0 , W_∞ are the initial and theoretical final widths of the coupler: $W_0 = 2r_1 + 2r_2$, $W_\infty = 2\sqrt{r_1^2 + r_2^2}$ and r_1 and r_2 are the initial radii of the fibers ($r_1 = r_2$ in the present test). The numerical simulations were performed on $400 \times 600 \mu\text{m}$ domain to minimize the impact of the boundaries. The physical properties that were used in the numerical simulations are given in Table I.

TABLE I. Physical properties of fused silica and air used for the validation procedure.

	ρ (kg/m ³)	μ (Pa s)	D (m ² /s)	σ (N/m)
Fused silica	2200	1.15×10^{5a}	1.51×10^{-14}	0.272^a
Air	0.185	6.01×10^{-5}		

^aViscosity and surface tension coefficients of the fused silica were adopted from Ref. [14].

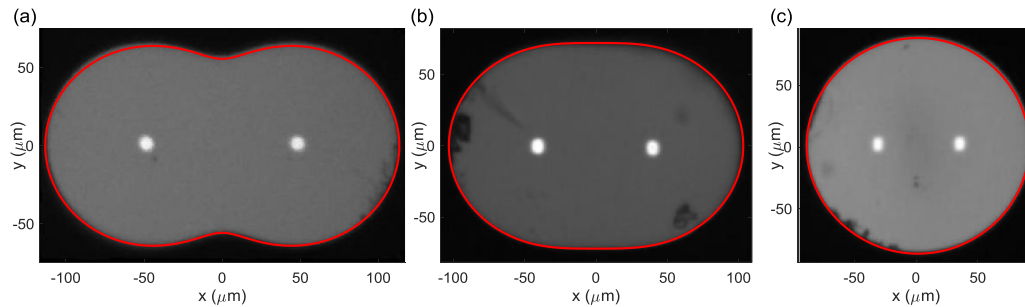


FIG. 4. Comparison of the simulation results (solid red line) obtained in the current work to the experimental results of Pone *et al.* [14]. The cross sections are at (a) $f = 0.355$, (b) $f = 0.6$, and (c) $f = 0.92$.

A comparison between the results obtained in the current work and those published in Ref. [14] is given in Fig. 4. The results depicted in Fig. 4 do indeed show good agreement between the current simulation and the measurements performed in Ref. [14]. Nonetheless, validation of the numerical method is still needed for more complex situations involving asymmetric structures, internal dopant flow, diffusion, and pulling, as will be discussed in subsequent sections.

VI. EXPERIMENTAL SETUP

The primary purpose of the experiments reported here was to test and validate the numerical methodology in complex situations and to study its accuracy and limitations. For this purpose, several fused fiber components were fabricated and analyzed. To fabricate the components, a commercial scanning hydrogen flame glass-processing workstation (Lighted CW-5000) was used. In all the test cases, except for one (in which a noncircular fiber was tested), two optical fibers were stripped, cleaned, and fixed in a holder, ensuring good physical contact between them (see Fig. 5). The fibers were then slowly pulled, while the scanning hydrogen flame provided the energy required to transform the glass into an effective viscous fluid. Scanning the flame back and forth along a preset length of the contacting fibers at a much higher rate than the pulling rate provided a zone of an effective constant temperature [32]. The flame was set to scan a total length of 10 mm at a rate of $500 \mu\text{m/s}$. The pulling rate was set to $0.75 \mu\text{m/s}$ (each side). The process was terminated after about 2 h when the pulled length had reached 10 mm. The temperature of the glass was approximated to be 1650°C .

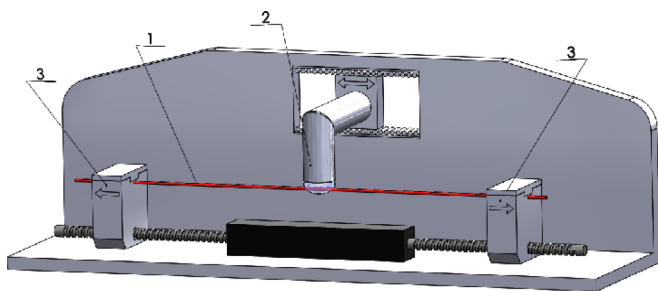


FIG. 5. Illustration of the glass-processing workstation. The main components are 1-optic fibers, 2-scanning flame, 3-pulling holders.

At the end of each fabrication process, the new optical fiber component was inserted into a U-shaped glass ferrule. The ferrule was filled with an epoxy resin and subjected to UV curing to form a rigid material encapsulating the fiber component, which was then placed in a holder positioned in a micrometer screw. Next, the end of the ferrule with its epoxy-immobilized fiber component was sliced off (using a turning diamond disk) and the cut end was polished (with a polishing sheet), as depicted in Fig. 6. The polished end was then examined under a microscope, and its cross-sectional shape was recorded with a camera. The process was repeated a number of times. Combining the photographs of the fused component along its longitudinal axis enabled a 3D reconstruction of its shape. To minimize the uncertainty as to the location of each cross-sectional measurement, slicing, polishing, and recording were performed using the same fixture.

To cover the wide spectrum of the parameters, the simulations and experimental analysis were performed and compared for four different types of components (see Fig. 7). The first—most basic component (coupler)—was prepared from two SMF-28 single-mode fibers ($125/8.2\text{-}\mu\text{m}$ cladding/core diameters) and was used for examining the fully symmetric configuration. The second type was composed of an SMF-28 fiber combined with a $125/106\text{-}\mu\text{m}$ diameter (cladding-core) fiber. In this case—referred to as the pump-SMF coupler later in the paper—the external interface of the coupler was symmetric, and the core refractive index of the fibers was not symmetric. The large core of the $125/106\text{-}\mu\text{m}$ fiber facilitated the tracking of the core interface. The third type of coupler constituted a fully nonsymmetric configuration produced from two fibers, one with a $125\text{-}\mu\text{m}$ outer cladding diameter and the other with an $80.3\text{-}\mu\text{m}$ outer cladding diameter. The fourth configuration had the most complex geometry—that of noncircular fiber tapering. Our working hypothesis for this study was that once the developed numerical methodology had been validated for accurate prediction of the characteristics typical of the four above configurations, it could also be used for the theoretical analysis of optical fibers having a wide variety of external shapes (other than those used here) and internal compositions.

VII. CALIBRATION AND SIMILARITY ANALYSIS

Prior to describing the series of numerical simulations and experiments that were conducted, we point out two major factors that can result in significant deviations between the numerical and the experimental results. The first factor

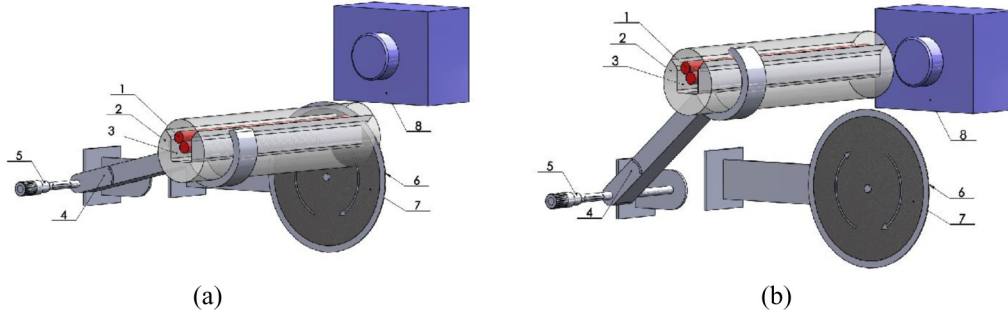


FIG. 6. The measurements setup. 1-fused coupler, 2-U-shaped glass, 3-epoxy resin, 4-holder, 5-micrometer screw, 6-edge of the rotating cutting disk, 7-rotating sandpaper, 8-camera. (a) The first step of measurements. The coupler was sliced and polished at a precise cross section. (b) The second step of measurements. The coupler's cross section was photographed.

is the strong dependence of the viscosity of fused silica on the temperature [33,34]. This is in contrast to the density ($\sim 2200 \text{ kg/m}^3$) and the surface tension coefficient ($\sim 0.3 \text{ N/m}$) of fused silica, known to be only slightly dependent on temperature variations [33]. To illustrate this factor, we present the time evolution of the degree of fusion, f , calculated for several values of the viscosity of the fused silica, as shown in Fig. 8. The time evolution was calculated for viscosity values lying in the range of $\mu = (5\text{--}50 \text{ GPa s})$, which corresponds to the typical range of working temperatures $T = (1800\text{--}1650 \text{ }^\circ\text{C})$, respectively. As can be seen from Fig. 8, the f values measured at the same time instance can deviate by up to fivefold, which stresses the need for careful calibration of the viscosity of the fused silica as a function of temperature. The second factor stems from strong dependency of the viscosity of fused silica on the absorption rate of hydroxides (OH) formed on the fiber surface during heating by the hydrogen flame [35]. This dependency can result in a significant deviation between the numerical and experimental results for long-term heating processes.

Since it is difficult to calculate and measure the OH concentration during the fabrication process, the time dependence of the viscosity μ of fused silica fibers subjected to a constant hydrogen flame, at a constant temperature, was approximated

by the following relation:

$$\mu(t) = (\mu_0 - \mu_s)e^{-\lambda t} + \mu_s, \quad (20)$$

where μ_0 , μ_s , and λ are the initial viscosity, the viscosity at the saturated state, and the OH absorption rate, respectively [35].

Significant variation of the viscosity values and the marked impact of this variation on the degree of fusion motivated us to perform a similarity analysis that would allow us to cancel out the dependence of the degree of fusion on the viscosity of the fused silica. The similarity was achieved by representing the degree of fusion as a function of the aspect ratio, H/W of the coupler, as defined in Fig. 9. As a result, the simulated degree of fusion was correlated with the aspect ratio of the coupler, regardless of the viscosity values (see Fig. 10).

In addition, to characterize the evolution of viscosity in the current experiments, the problem was simulated with several initial and saturated viscosities and different OH absorption rates. It was found that the values of $\mu_0 = 50 \text{ GPa s}$, $\mu_s = 5 \text{ GPa s}$, and $\lambda = 6 \times 10^{-4} \text{ s}^{-1}$ provide the best correlation with the experimental results.

In contrast to the degree of fusion determined by Eq. (19), the pulling rate was not equal to zero in the current experiments and simulations, and therefore W_0 and W_∞ were not constant during the process and had to be evaluated at each time instance for each cross section. The relationship between W and the cross-sectional area is given by $[W_0(t), W_\infty(t)] \propto \sqrt{A(t)}$, and hence the modified fusion degree is expressed by

$$f_m = \frac{W_0(t) - W(t)}{W_0(t) - W_\infty(t)}, \quad (21)$$

where $W_0(t) = \frac{W_0(0)}{\sqrt{A_0}} \sqrt{A(t)}$ and $W_\infty(t) = \frac{2}{\sqrt{\pi}} \sqrt{A(t)}$. In the current experiments, the area $A(t)$ and the width $W(t)$ were measured to evaluate the modified fusion degree for each cross

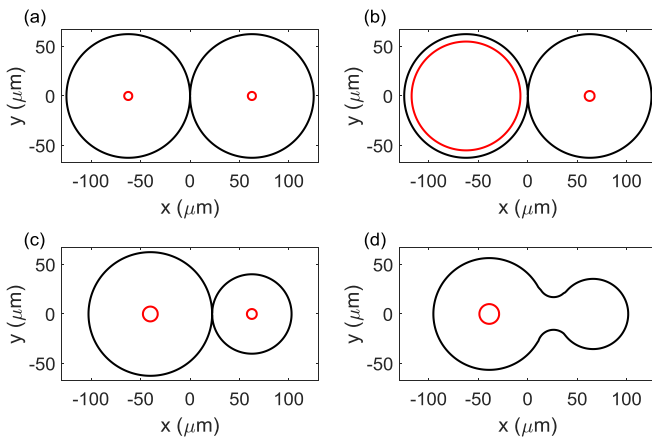


FIG. 7. Initial configurations of the analyzed cases; the black lines represent the external interface and the red line shows the shape of the initial core: (a) fully symmetric case, (b) symmetry only of the external interface, (c) nonsymmetric case, and (d) complex geometry.

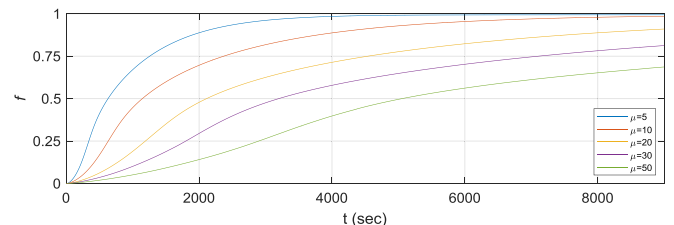


FIG. 8. Time evolution of the degree of fusion for several values of the viscosity (in GPa s, $v_s = 0$).

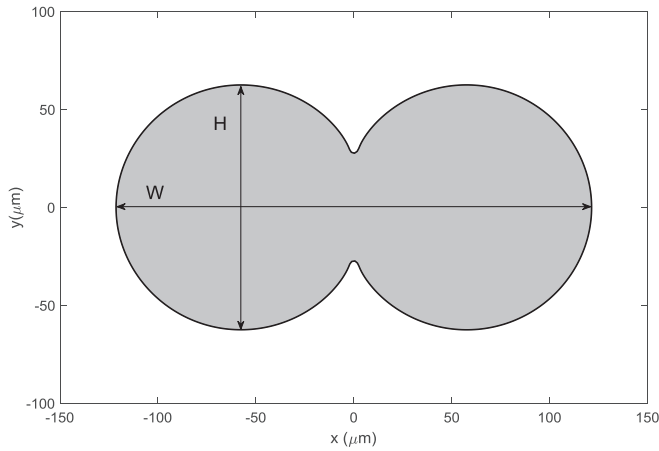


FIG. 9. Geometric dimensions of a typical coupler.

section, and the height $H(t)$ was measured to calculate the aspect ratio of the coupler [$H(t)/W(t)$].

VIII. RESULTS AND DISCUSSION

All the numerical simulations were performed for a computational domain of size $400 \times 600 \mu\text{m}$, while the grid resolution was 675×450 . The boundary conditions utilized in the numerical simulations were the Dirichlet boundary condition for pressure and a zero gradient value for all the velocity components at all four edges of the computational domain. The initial values of the concentration in the numerical simulations were set to unity, representing the normalized value related to the initial concentration. The experimental analysis and the simulation results are presented and discussed in the following sections.

A number of representative simulations were also performed on a 1350×900 grid in the framework of a grid independence study. It was found that the discrepancy between the degrees of fusion obtained on the two grids did not exceed 3%, thus allowing us to perform all the simulations on the 675×450 grid. Remarkably, the maximal discrepancy between the results obtained on the two grids was observed at the beginning of the numerical simulations as a result of exceptionally high values of the interface curvature at the point of contact between the two fibers. The dimensional computational time step used in all the simulations was equal to 10 s.

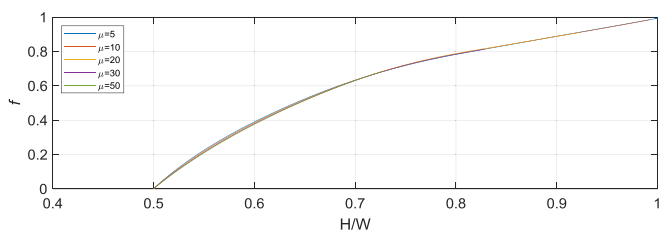


FIG. 10. Evolution of the degree of fusion for several viscosity values (in GPa s) as a function of the aspect ratio H/W of the coupler ($v_s = 0$).

A. Comparison between the numerical simulations and the experimental results

1. Symmetric two-single mode fiber (SMF) coupler

A qualitative comparison between the experimentally and numerically obtained external shapes of the coupler and the spatiotemporal distribution of the dopant within the coupler’s core—determining the refractive index profile (under the assumption of linear dependence of the dopant concentration on the refractive index)—is given in Fig. 11.

As can be seen from Fig. 11, a good correlation was found between the experimentally and numerically obtained external boundaries of the coupler for the entire range of time instances. Additionally, an acceptable qualitative agreement between the distribution of the dopants in the core of each fiber allowed reliable prediction of their spatiotemporal concentration distribution and the refractive index profile. Note that the glare areas clearly visible on the photographs acquired in the course of experiments were generated by an external light source. As such, the areas constitute only qualitative characteristics of the spatial distribution of the dopants. Nonetheless, the numerical results predict a significant (between 4- and 10-fold) decay of the peak concentration values with time (see the fourth column in Fig. 11).

A quantitative comparison between the numerically and experimentally obtained evolution areas and the modified fusion degree [see Eq. (21)] is given in Fig. 12. It can be seen from the figure that the numerically obtained temporal evolutions of the area and the modified fusion degree are cross correlated with the corresponding experimentally measured values for the entire range of time instances, which successfully validates the developed quasi-3D model. We note in passing that at the beginning of the numerical simulations very small [$0(10^{-3})$], but still negative values, of the modified fusion degree were obtained. This unphysical result may be attributed to the numerical error resulting from exceptionally high values of the interface curvature and could be corrected by applying simple filtering, replacing the negative unphysical values by zero.

We next present the numerically and experimentally obtained results correlating the modified fusion degree with the height to width ratio of the coupler, as shown in Fig. 13. Good agreement between the numerical and experimental results was obtained. Note that the results shown in Fig. 13 are invariant to the viscosity values. The presented modified fusion degree–(height–width) ratio relationship directly affects the overall fusion time and indirectly effects the distribution of the core dopants. The graph in Fig. 13 may assist coupler design by serving as a preliminary tool for estimating the modified fusion degree from the external dimensions of the fibers.

2. Pump-SMF coupler

The pump-SMF coupler configuration is characterized by a symmetric external shape, while the core of one of the fibers is much bigger than the core of its counterpart. This setup allows for more efficient tracking of the experimentally acquired data regarding the spatiotemporal distribution of the dopants in the cores. A comparison between the simulation and the experimental results acquired at four different time instances revealed acceptable agreement between the numerically and

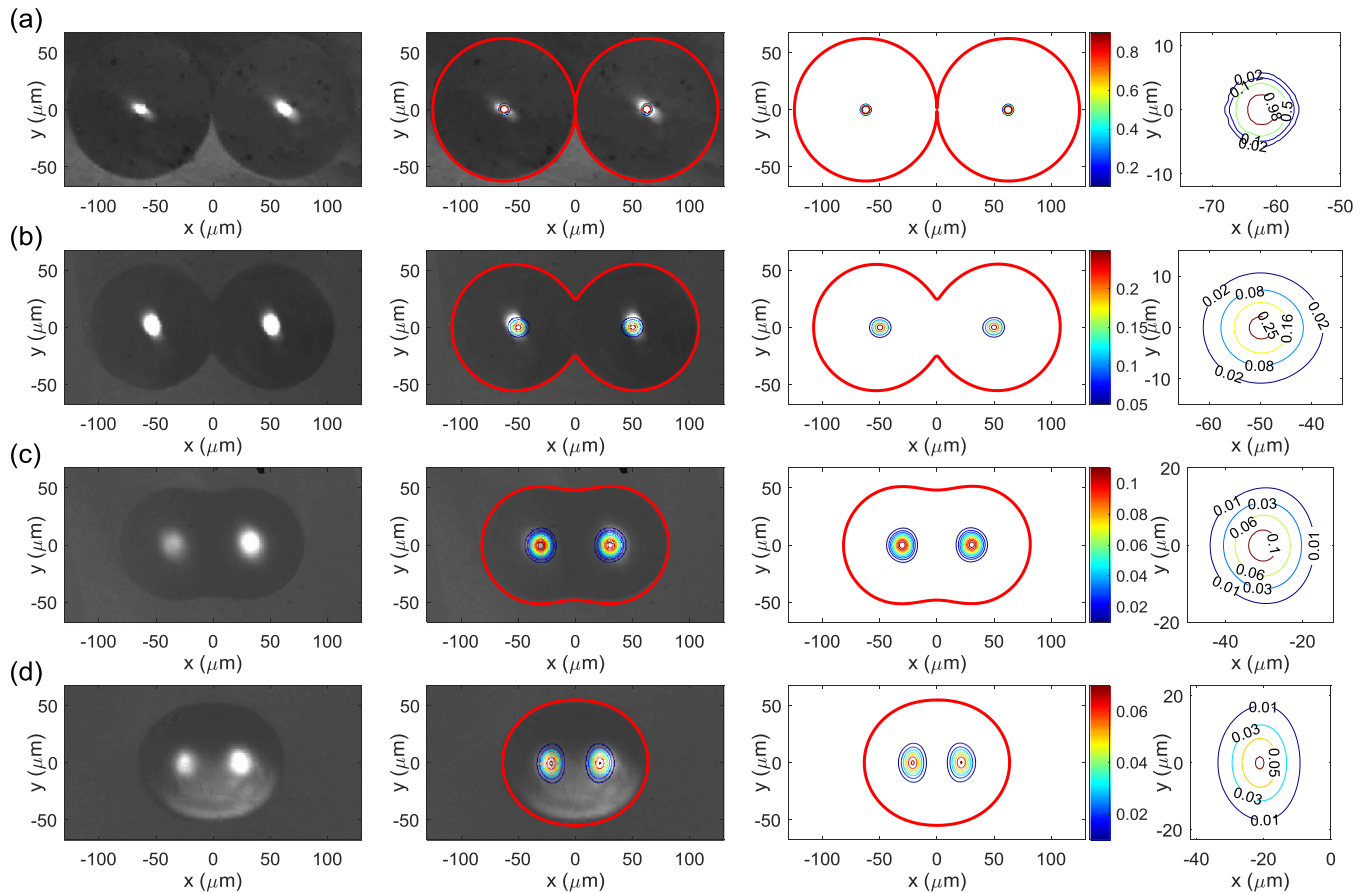


FIG. 11. Experimentally and numerically obtained cross sections of a fully symmetric SMF fiber coupler at different time instances: (a) 30 s, (b) 1650 s, (c) 3600 s, and (d) 5300 s. Columns 1 and 3 show the experimental and simulation results, respectively; column 2 shows a superposition of columns 1 and 3; and column 4 shows close-ups of the numerically predicted core area of the left fiber.

experimentally obtained characteristics of the coupler for the entire range of time instances (see Fig. 14). In contrast to the simple configuration, the core of the left fiber intersects the vertical centerline crossing the domain at $x = 0$ in the course of the fusion process [see Fig. 14(d)]. Note that from a numerical point of view, the observed spatial expansion of the core of the left fiber was attributed to the molecular

diffusion resulting from one-way coupling between the NS [Eq. (5)] and convection-diffusion [Eq. (6)] equations. The assumption of one-way coupling adopted in the current study was validated by the good qualitative agreement obtained between the experimentally and numerically obtained spatiotemporal distributions of the dopants in the coupler core. The obtained results also successfully verified the correctness of the implementation of the boundary conditions applied to the coupler boundary aiming at providing zero concentration flux of the dopants out of the coupler. Figure 15 presents a quantitative comparison between the numerically and experimentally obtained temporal evolutions of the coupler area and

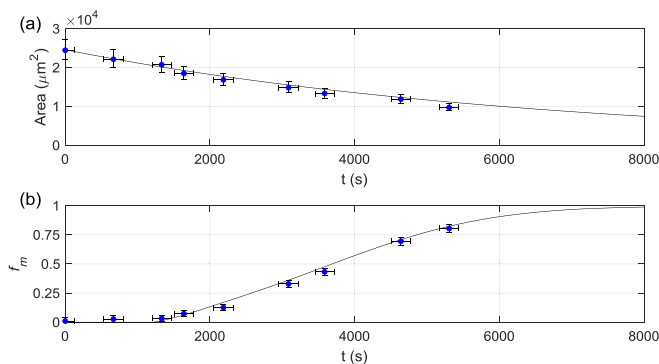


FIG. 12. Comparison between the numerically and experimentally obtained temporal evolutions of the cross-sectional area and the modified fusion degree typical of the symmetric coupler. Line-simulation results; points-experimental results. (a) The decrease in area with time. (b) Temporal evolution of the modified fusion degree.

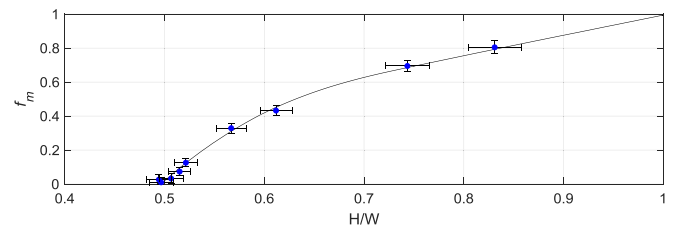


FIG. 13. Comparison between the numerically and experimentally obtained temporal evolutions of the modified fusion degree as a function of the coupler dimensions. Line-simulation results; points-experimental results.

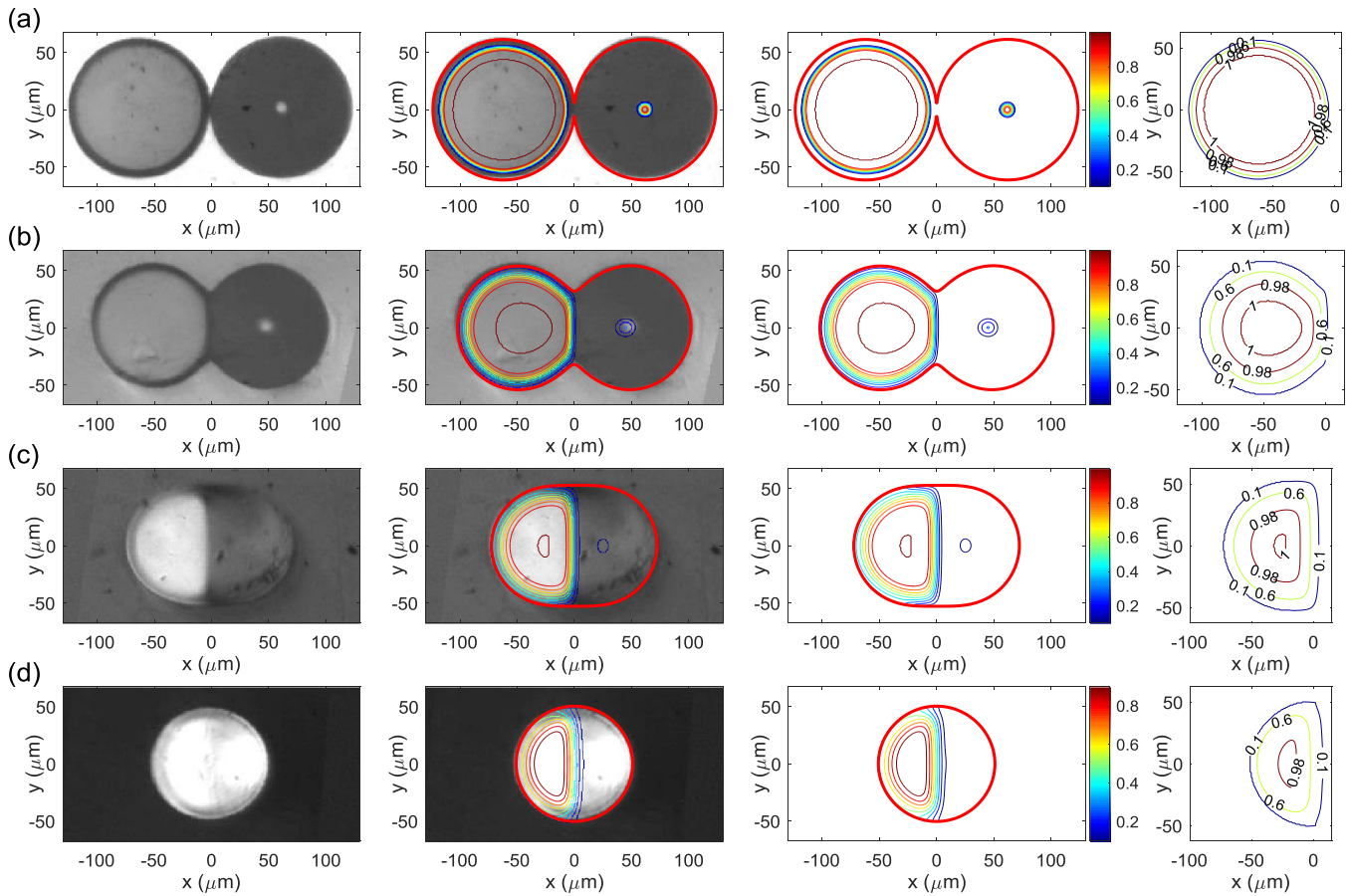


FIG. 14. Experimentally and numerically obtained cross sections of the *pump* (125/106 μm) and *SMF* (125/8 μm) fibers coupler at different time instants: (a) 210 s, (b) 2100 s, (c) 4400 s, and (d) 7500 s. Columns 1 and 3 show the experimental and simulation results, respectively; column 2 shows a superposition of columns 1 and 3; and column 4 shows close-ups of the numerically predicted core area of the left fiber.

the modified fusion degree. It can be seen from Fig. 15(a) that for most of the time instances, the experimentally measured area is slightly larger than that predicted numerically. A possible reason for this discrepancy could be that the fibers were not fixed tight enough in their holders to avoid slight sliding at the beginning of the fabrication process prior to tapering.

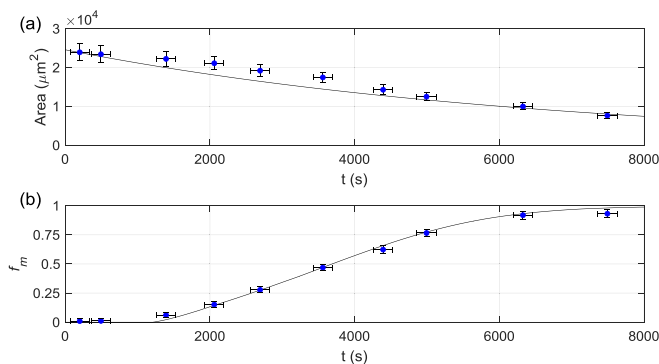


FIG. 15. Comparison between the numerically and the experimentally obtained temporal evolutions of the cross-sectional area and the modified fusion degree typical of the second test case. Line-simulation results; points-experimental results. (a) The decrease in area with time. (b) Temporal evolution of the modified fusion degree.

Note that, despite the discrepancy in the cross-sectional areas, the correlation between the coupler aspect ratio H/W and the modified fusion degree was preserved, as shown in Fig. 16. For this reason, the experimentally acquired photographs presented in Figs. 14(b) and 14(c) were downscaled by up to 5%.

3. Nonsymmetric coupler

The nonsymmetric coupler was prepared by fusing fibers with outer cladding diameters of 125 and 80 μm . Comparisons of the experimental and numerical results demonstrated good qualitative agreement for both the outer shape and

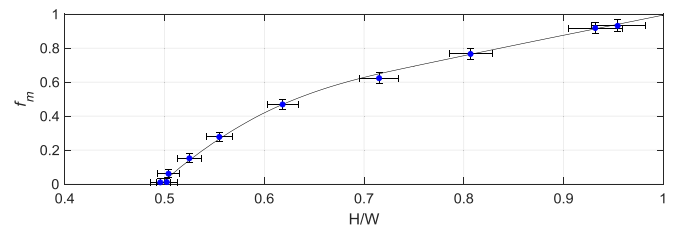


FIG. 16. Comparison between the numerically and the experimentally obtained temporal evolutions of the modified fusion degree as a function of the coupler dimensions for the second test case. Line-simulation results; points-experimental results.

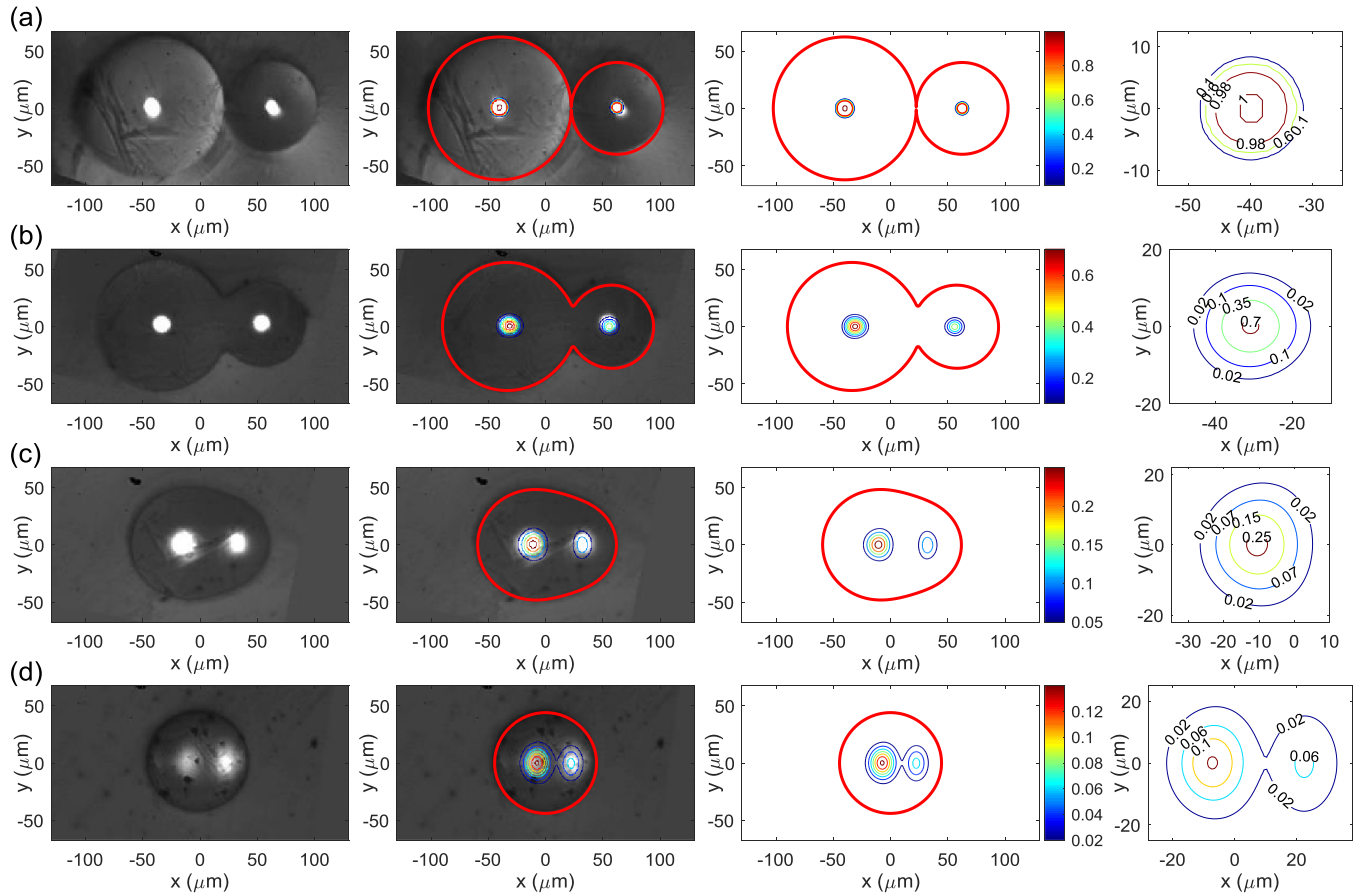


FIG. 17. Experimentally and numerically obtained cross sections of the nonsymmetric coupler at different time instances: (a) 30 s, (b) 1350 s, (c) 4300 s, and (d) 7000 s. Columns 1 and 3 show the experimental and simulation results, respectively; column 2 shows a superposition of columns 1 and 3; and column 4 shows close-ups of the numerically predicted core area of the left fiber.

the spatial distribution of the dopants (see Fig. 17) and for the temporal evolution of the cross-sectional areas [see Fig. 18(a)]. Agreement between the experimentally and numerically obtained time evolutions of the modified fusion degree was not as good as that for the areas [see Fig. 18(a) vs 18(b)]: the discrepancies between the values were particu-

larly marked at the beginning and end of the fusion process, reaching 70 and 10%, respectively. This observation may indicate overestimation of the viscosity values utilized in the numerical simulations compared to the actual viscosities in the experiments, which resulted in a smoother evolution of the modified fusion degree in the numerical simulations. Remarkably, the above notwithstanding, acceptable agreement was obtained between experimentally and numerically obtained values of the modified fusion degree as a function of the coupler cross-section size (see Fig. 19). These results indicate that the temporal evolution of the cross-sectional area is primarily determined by the initial geometry of the fibers, while the

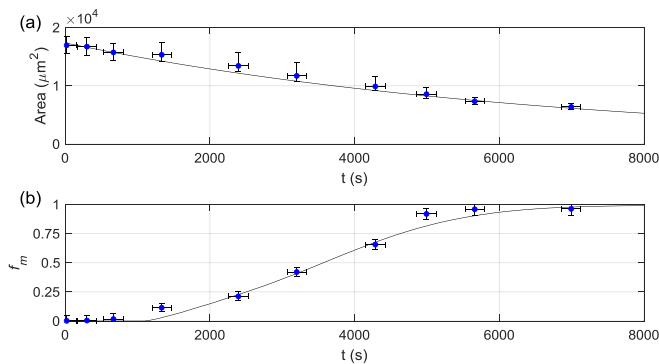


FIG. 18. Comparison between the numerically and experimentally obtained temporal evolutions of the cross-sectional area and the modified fusion degree typical of the nonsymmetric coupler. Line—simulation results; points—experimental results. (a) The decrease in area with time. (b) Temporal evolution of the modified fusion degree.

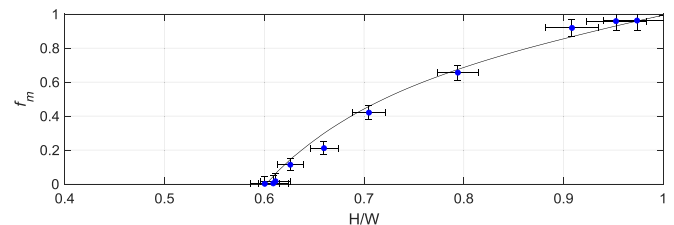


FIG. 19. Comparison between the numerically and experimentally obtained temporal evolutions of the modified fusion degree as a function of the coupler dimensions for the nonsymmetric coupler. Line—simulation results; points—experimental results.

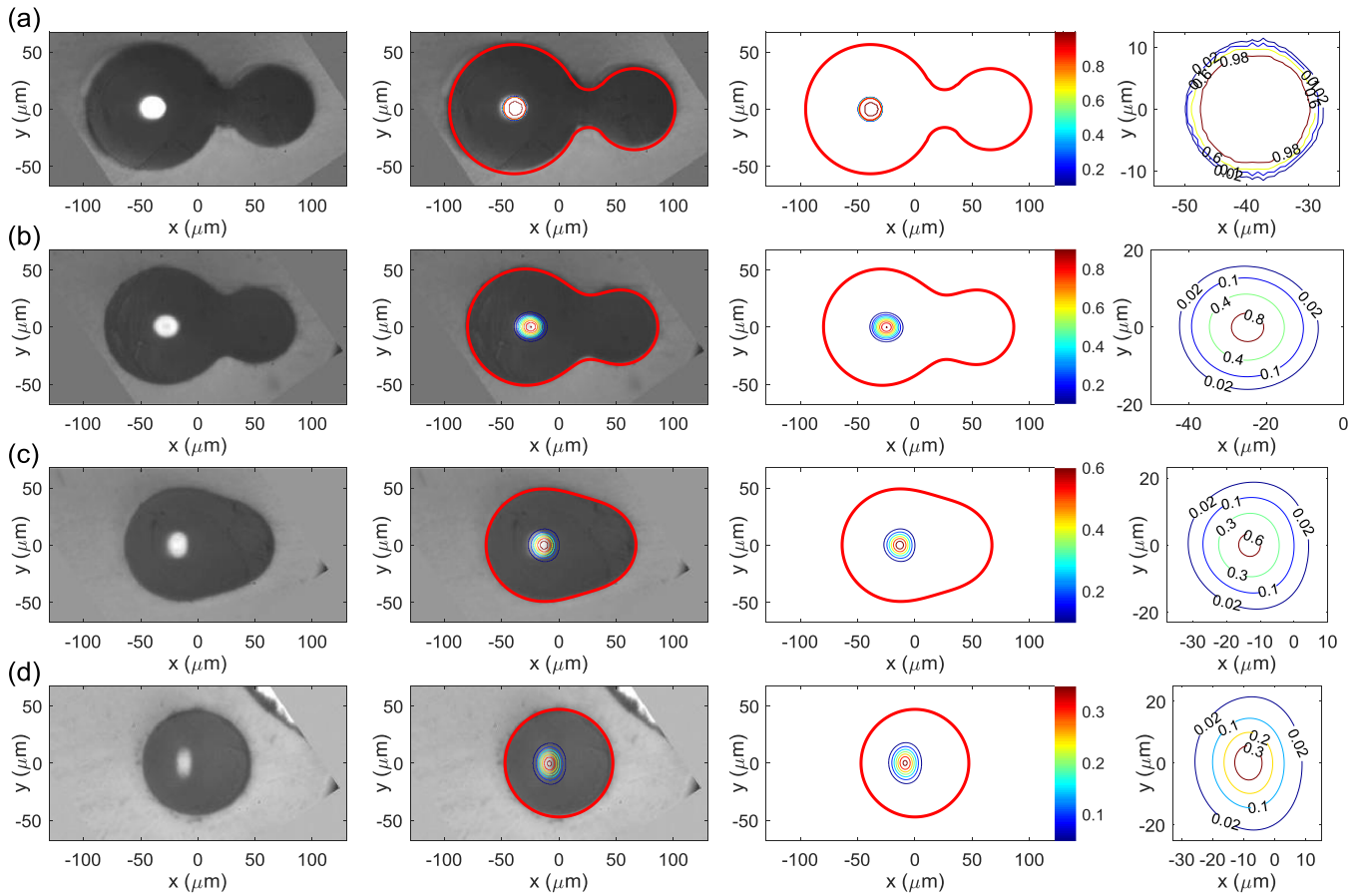


FIG. 20. Experimentally and numerically obtained cross sections of the noncircular tapered fiber coupler at different time instances: (a) 10 s, (b) 1320 s, (c) 2500 s, and (d) 5000 s. Columns 1 and 3 show the experimental and simulation results, respectively; column 2 shows a superposition of columns 1 and 3; and column 4 shows close-ups of the numerically predicted core area of the left fiber.

values of the viscosity and the pulling rate affect the duration of the overall process.

4. Fiber with a noncircular cross section

The custom-made fiber investigated in this section was characterized by a noncircular cross section along its entire longitudinal axis [see Fig. 20(a)]. In contrast to the previous configurations, the viscosity values at the initial and saturated states were equal to $\mu_0 = 20$ GPa s and $\mu_s = 2$ GPa s, respectively, while the value of the OH absorption rate was equal to $\lambda = 6 \times 10^{-4} \text{ s}^{-1}$ (the same as that for the previous configurations). Generally speaking, this kind of fiber fulfills its optical purpose in its present form and should not be tapered. Nonetheless, the current test case was processed for the validation purposes of the developed numerical tool. A comparison between the numerically and experimentally obtained results revealed good qualitative agreement between the temporal evolutions of the outer shapes of the fiber for all the time instances (see Fig. 20). Good agreement for all the time instances was also apparent in a comparison between the numerical and experimental spatiotemporal evolutions of the concentrations of the dopants. Figure 21 shows a good correlation between the numerical and experimental results of the cross-sectional area and the modified fusion degree time evolutions. Moreover, in this configuration, the time required

to obtain full fusion ($f_m = 1$), is much faster than that for the other test cases, where the viscosity values were higher. Figure 22 also shows the excellent compatibility between the experimentally and numerically obtained values for the

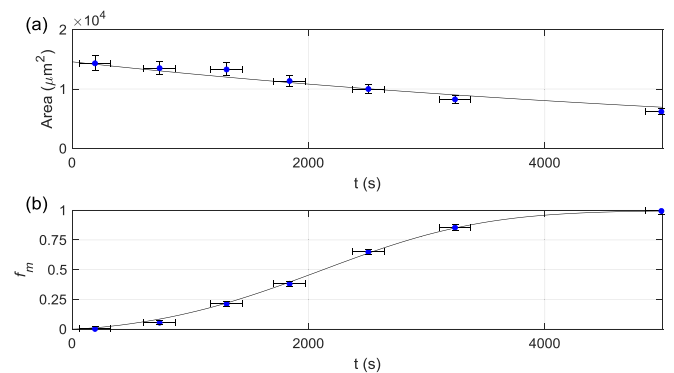


FIG. 21. Comparison between the numerically and experimentally obtained temporal evolutions of the cross-sectional area and the modified fusion degree typical of a fiber with a noncircular cross section during tapering. Line-simulation results; points-experimental results. (a) The decrease in area with time. (b) Temporal evolution of the modified fusion degree.

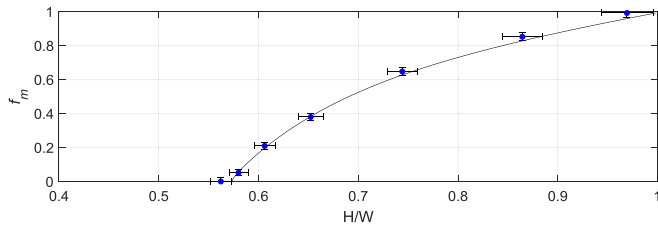


FIG. 22. Comparison between the numerically and experimentally obtained temporal evolutions of the modified fusion degree as a function of the coupler dimensions for a fiber with a noncircular cross section. Line-simulation results; points-experimental results.

temporal evolution of the modified fusion degree as a function of the coupler dimensions.

Figure 23 shows the full 3D shapes of the four types of optical components by superpositioning several cross sections simulated at a number of consecutive time instances. This kind of data may serve as input for optical numerical simulation packages, such as OPTICWAVE, RSOFTE, and COMSOL, which can predict the optical performance of the component (such simulations are beyond the scope of this study). Note that the smaller the initial cross-sectional area of the core, the more rapid is the decay of the corresponding concentration peak values of the dopants.

B. Characterization of the nonsymmetric couplers

In the course of the simulations, it was found that the viscosity values have a considerable effect on the overall time required to achieve the complete fusion between the fibers and to provide diffusion of the dopants. It was also found that the values of the aspect ratio H/W and the modified fusion degree are almost not affected by variations in the viscosity. For this reason, we simulated several configurations of nonsymmetric couplers characterized by various H/W aspect ratios.

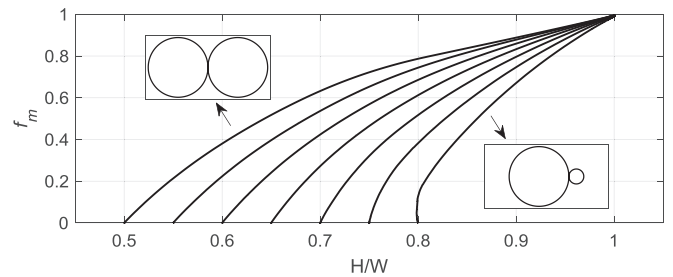


FIG. 24. Simulation results of the modified fusion degree related to the height-width (H/W) ratio of the coupler for several initial ratios.

Figure 24 presents seven curves, each related to a different initial value of H/W , starting from the symmetric case characterized by a value of $H/W = 0.5$ and ending with the strongly nonsymmetric coupler characterized by a value of $H/W = 0.8$. As mentioned above, the mapping so obtained can be used as a preliminary tool used for the design of couplers, as it facilitates the evaluation of the modified fusion degree by simple measurements. As can be seen from Fig. 24, for all the cases, the modified fusion degree started from zero and increased up to unity. It may also be seen that a higher initial value of H/W resulted in faster growth of the modified fusion degree, apparently as a consequence of the higher surface tension forces prevailing throughout the fusion process, in turn, as a result of higher curvature values typical of fibers with smaller cross sections.

C. Advanced modeling of multifiber combiners

The developed numerical tool can also successfully handle the time evolution of much more complex multifiber configurations, incorporating many contact points for each fiber and also including the non-negligible amount of air trapped

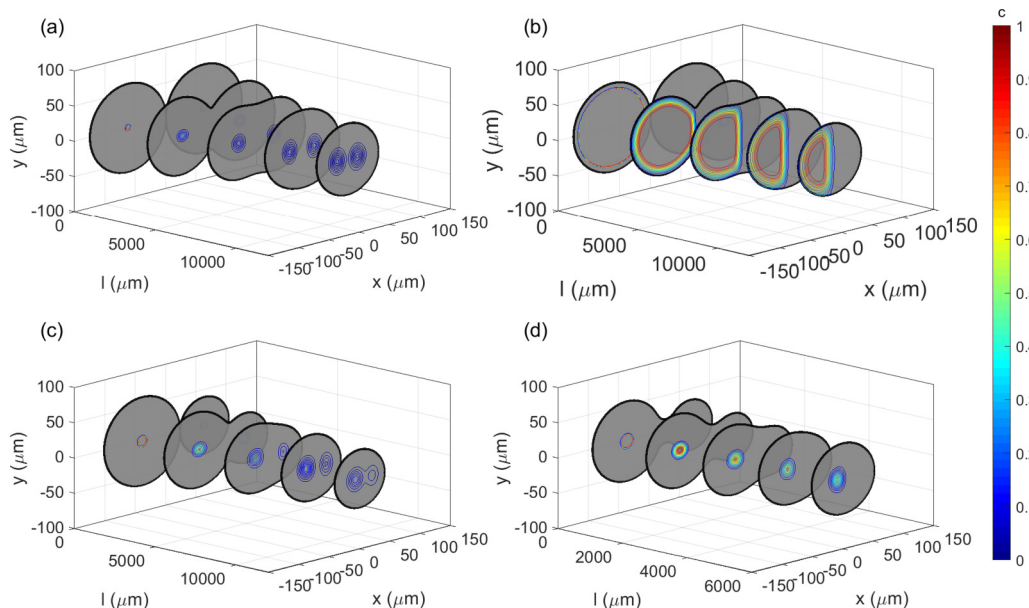


FIG. 23. Simulated 3D structure of: (a) a symmetric coupler, (b) a coupler composed of pump (125/106 μm) and SMF (125/8 μm) fibers, (c) a nonsymmetric coupler, and (d) a tapered noncircular fiber. Each cross section was obtained at different time instances.

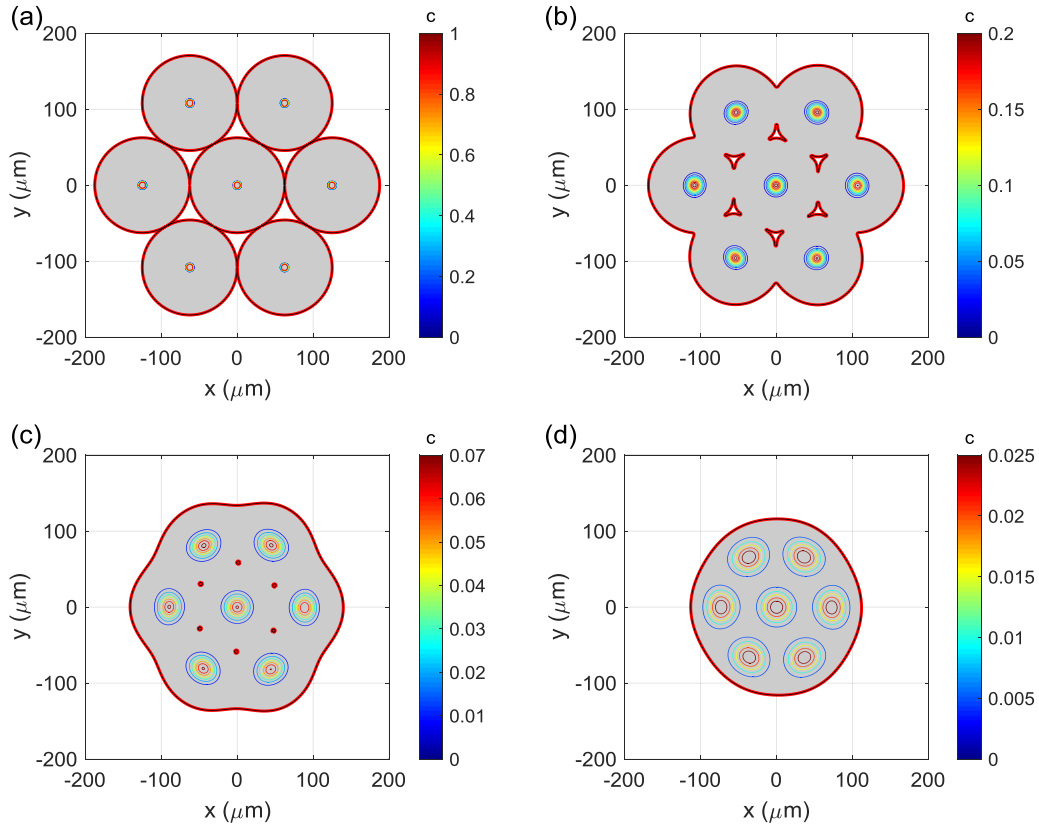


FIG. 25. Simulation results for a combiner composed of seven fibers at times: (a) Initial state, (b) 900 s, (c) 2500 s, and (d) 5000 s.

between the boundaries of adjacent fibers. A representative example of such simulation is demonstrated in Fig. 25, for an optical combiner composed of seven fibers arranged as six fibers circling a central fiber; each fiber touches its neighbor at a single contact point, such that the central fiber has six contact points with all the surrounding fibers, and each external fiber has three contact points with its immediate neighbors. The physical properties of the fiber material are the same as those utilized for the first three configurations (see Sec. VII). In the course of the numerical simulation, the area of air trapped between the boundaries of the neighboring fibers decreases until total termination of the air regions. The process is simulated explicitly by controlling the air pull-out rate implemented as a distributed sink [Eq. (4)] for each air-trapped region. The time evolution of the air-trapped regions and of the external interface of the combiner is governed by the solution of the continuity and NS equations [Eqs. (4) and (5)].

It can be seen that in the first stage of the production process, the peripheral fibers evolve nonaxisymmetrically (although the periodicity is preserved) due to the initially non-axisymmetric geometry of the air-fiber interface and the air regions trapped between the peripheral and the central fibers. As the tapering progresses, the regions of trapped air are eliminated, and the external shape of the component is smoothed out by the surface tension force, causing the shape of the component to eventually approach a circular configuration. Note that the similar shapes were obtained experimentally by Ref. [36].

IX. SUMMARY AND CONCLUSIONS

A numerical tool for simulation of the structural evolution of fused fiber-optic components based on the immersed boundary method and a front-tracking approach was developed. The tool was extensively cross validated by comparison with experimental data. It was demonstrated that the tool can be applied for reliable spatiotemporal prediction both for the external shape of the fiber components and for the internal dopants concentration.

The numerical model is based on a quasi-3D approximation used to simulate the fabrication of typical optical components by the heat and pull technique. In particular, at each discrete time instance, the time evolution of a specific cross section of the three-dimensional component can be simulated by the solution of 2D incompressible isothermal NS equations. The decrease of cross-section area of a component with time resulted by the pulling process was modeled by introducing a distributed source.

The quasi-3D approximation was successfully validated by comparing the numerically predicted external shapes with their experimentally obtained counterparts for four representative optical couplers. The quasi-3D approximation was also validated by comparison of the numerically and experimentally obtained distributions of the dopant concentrations within the coupler cores, which play a significant role in determining the refractive index profile of each coupler. It was found that the dopant diffusion within the coupler core plays an essential role in the overall structure of the coupler and cannot be neglected in numerical simulations.

A comparison of the numerical and experimental results also revealed that the viscosity of the fused silica dropped during the fabrication process, despite insignificant temperature variations. This observation may be attributed to the absorption of OH (hydroxyl) in fused silica when the last is exposed to hydrogen flame. It is thus essential that the change in the viscosity of the fused silica due to OH absorption be considered when a hydrogen flame is used to fabricate fused optical components.

The numerical characterization of the structural evolution of couplers was also performed for several nonsymmetrical cases, showing that it is possible to evaluate the degree of fusion of a given optical coupler by only measuring its height and width. Finally, a numerical simulation to predict the spatiotemporal evolution of a fused seven-fiber combiner was presented. This simulation showed that the numerical tool can handle complex geometries and may be used to develop a wide range of fused optical fiber components.

- [1] D. Noordegraaf, P. M. Skovgaard, M. D. Nielsen, and J. Bland-Hawthorn, Efficient multi-mode to single-mode coupling in a photonic lantern, *Opt. Express* **17**, 1988 (2009).
- [2] Z. S. Eznaveh, L. J. Antonio, J. A. Zacarias, A. Schulzgen, C. Okonkwo, and R. A. Correa, All-fiber few-mode multicore photonic lantern mode multiplexer, *Opt. Express* **25**, 16701 (2017).
- [3] S. Dong, H. Ding, Y. Liu, and X. Qi, Investigation of evanescent coupling between tapered fiber and a multimode slab waveguide, *Appl. Opt.* **51**, C152 (2012).
- [4] S. G. Leon-Saval, A. Argyros, and J. Bland-Hawthorn, Photonic lanterns, *Nanophotonics* **2**, 429 (2013).
- [5] K. Li, T. Zhang, G. Liu, N. Zhang, M. Zhang, and L. Wei, Ultrasensitive optical microfiber coupler based sensors operating near the turning point of effective group index difference, *Appl. Phys. Lett.* **109**, 101101 (2016).
- [6] S. Lacroix, F. Gonthier, and J. Bures, Modeling of symmetric 2X2 fused-fiber couplers, *Appl. Opt.* **33**, 8361 (1994).
- [7] P. Garabedian, Free boundary flows of a viscous liquid, *Commun. Pure Appl. Math.* **19**, 421 (1966).
- [8] S. Richardson, Two-dimensional bubbles in slow viscous flows, *J. Fluid Mech.* **33**, 475 (1968).
- [9] S. Richardson, Two-dimensional bubbles in slow viscous flows. Part 2, *J. Fluid Mech.* **58**, 115 (1973).
- [10] S. Richardson, Two-dimensional slow viscous flows with time-dependent free boundaries driven by surface tension, *Eur. J. Appl. Math.* **3**, 193 (1992).
- [11] R. W. Hopper, Plane Stokes flow driven by capillarity on a free surface, *J. Fluid Mech.* **213**, 349 (1990).
- [12] R. W. Hopper, Coalescence of two viscous cylinders by capillarity: Part I, theory, *J. Am. Ceram. Soc.* **76**, 2947 (1993).
- [13] R. W. Hopper, Coalescence of two viscous cylinders by capillarity: Part II, Shape evolution, *J. Am. Ceram. Soc.* **76**, 2953 (1993).
- [14] E. Pone, X. Daxhelet, and S. Lacroix, Refractive index profile of fused-fiber couplers cross-section, *Opt. Express* **12**, 1036 (2004).
- [15] E. Pone, X. Daxhelet, and S. Lacroix, Refractive index profile of fused-tapered fiber couplers, *Opt. Express* **12**, 2909 (2004).
- [16] S. Richardson, Two-dimensional Stokes flows with time-dependent free boundaries driven by surface tension, *Eur. J. Appl. Math.* **8**, 311 (1997).
- [17] T. Kikteva, D. Star, Z. Zhao, T. Baisley, and G. Leach, Molecular orientation, aggregation, and order in rhodamine films at the fused silica/air, *J. Phys. Chem. B* **103**, 1124 (1999).
- [18] V. Lou, R. Sato, and M. Tomozawa, Hydrogen diffusion in fused silica at high temperatures, *J. Non-Cryst. Solids* **315**, 13 (2003).
- [19] Y. Li, E. Jung, W. Lee, H. G. Lee, and J. Kim, Volume preserving immersed boundary methods for two-phase fluid flows, *Int. J. Numer. Methods Fluids* **69**, 842 (2012).
- [20] A. M. Roma, C. S. Peskin, and M. J. Berger, An adaptive version of the immersed boundary method, *J. Comput. Phys.* **153**, 509 (1999).
- [21] A. Spizzichino, S. Goldring, and Y. Feldman, The immersed boundary method: Application to two-phase immiscible flows, *Commun. Comput. Phys.* **25**, 107 (2019).
- [22] Y. Feldman, Semi-implicit direct forcing immersed boundary method for incompressible viscous thermal flow problems: A Schur complement approach, *Int. J. Heat Mass Transfer* **127**, 1267 (2018).
- [23] T. Kempe and F. Jochen, An improved immersed boundary method with direct forcing for the simulation of particle laden flows, *J. Comput. Phys.* **231**, 3663 (2012).
- [24] K. Taira and T. Colonius, The immersed boundary method: A projection approach, *J. Comput. Phys.* **225**, 2118 (2007).
- [25] Y. Feldman and Y. Gulberg, An extension of the immersed boundary method based on the distributed Lagrange multiplier approach, *J. Comput. Phys.* **322**, 248 (2016).
- [26] M. Uhlmann, An immersed boundary method with direct forcing for the simulation of particulate flows, *J. Comput. Phys.* **209**, 448 (2005).
- [27] G. Tryggvason, B. Bunner, A. Esmaeeli, D. Juric, N. Al-Rawahi, W. Tauber, J. Han, S. Nas, and Y. J. Jan, A Front tracking method for the computations of multiphase flow, *J. Comput. Phys.* **169**, 708 (2001).
- [28] G. Tryggvason, R. Scardovelli, and S. Zaleski, *Direct Numerical Simulations of Gas-Liquid Multiphase Flows* (Cambridge University Press, Cambridge, 2011).
- [29] S. Patankar, *Numerical Heat Transfer and Fluid Flow* (CRC Press, Boca Raton, FL, 1980).
- [30] P. R. Amestoy, I. S. Duff, J.-Y. L'Excellent, and J. Koster, A fully asynchronous multifrontal solver using distributed dynamic scheduling, *SIAM J. Matrix Anal. Appl.* **23**, 15 (2001).
- [31] P. R. Amestoy, A. Buttari, J.-Y. L'Excellent, and T. Mary, Performance and scalability of the block low-rank multifrontal factorization on multicore architectures, *ACM Trans. Math. Software* **45**, 1 (2019).
- [32] T. A. Birks and Y. W. Li, The shape of fiber tapers, *J. Lightwave Technol.* **10**, 432 (1992).
- [33] A. D. Yablon, *Optical Fiber Fusion Splicing* (Springer, Berlin, 2005), Vol. 103.
- [34] N. P. Bansal and R. H. Doremus, *Handbook of Glass Properties* (Academic Press Inc., London, 2013).
- [35] Y. Kikuchi, H. Sudo, and N. Kuzuu, OH content dependence of viscosity of Vitreous Silica, *J. Ceram. Soc. Japan* **105**, 645 (1997).
- [36] Y. Shamir, Y. Sintov, and M. Shtauf, Beam quality analysis and optimization in an adiabatic low mode tapered fiber beam combiner, *Opt. Soc. Am.* **27**, 2669 (2010).